ADVANCED MATERIALS
www.advmat.de

Acoustic Crystallization of 2D Colloidal Crystals

*Johannes Menath, Reza Mohammadi, Jens Christian Grauer, Claudius Deters, Maike Böhm, Benno Liebchen, Liesbeth M. C. Janssen, Hartmut Löwen, and Nicolas Vogel**

2D colloidal crystallization provides a simple strategy to produce defined nanostructure arrays over macroscopic areas. Regularity and long-range order of such crystals is essential to ensure functionality, but difficult to achieve in self-assembling systems. Here, a simple loudspeaker setup for the acoustic crystallization of 2D colloidal crystals (ACDC) of polystyrene, microgels, and core–shell particles at liquid interfaces is introduced. This setup anneals an interfacial colloidal monolayer and affords an increase in average grain size by almost two orders of magnitude. The order is characterized via the structural color of the colloidal crystal, the acoustic annealing process is optimized via the frequency and the amplitude of the applied sound wave, and its efficiency is rationalized via the surface coverage-dependent interactions within the interfacial colloidal monolayer. Computer simulations show that multiple rearrangement mechanisms at different length scales, from the local motion around voids to grain boundary movements via consecutive particle rotations around common centers, collude to remove defects. The experimentally simple ACDC process, paired with the demonstrated applicability toward complex particle systems, provides access to highly defined nanostructure arrays for a wide range of research communities.

1. Introduction

Colloidal assemblies are ideal model systems to study crystallization phenomena,[1–4] and also serve as an important platform to create functional nanostructures from the bottom up.[5,6] The constituent colloidal particles are highly appealing for fundamental research as they can be synthesized with high control of shape, size, and polydispersity, and can be made sufficiently large to enable direct observation of their phase behavior by optical microscopy.[7,8] In this regard, liquid interfaces are ideal templates to tailor colloidal self-assembly processes. Colloidal particles strongly adsorb to liquid interfaces and can form well-ordered structures.[9–11] The liquid interface itself confines the particles into 2D, facilitating control and observation. It also influences the interactions between the particles via additional repulsive dipole[12,13] and capillary forces,[14–16] or via the deformation of soft particles,[17,18] and can therefore be used to control the phase behavior[19,20] and the resulting assembly structure.[21–25]

The formed interfacial assemblies can be transferred to a desired solid substrate, yielding nanoparticle arrays over large areas without requiring any sophisticated nanofabrication equipment or clean-room infrastructure.[10,11,26,27] These colloidal monolayers are widely used as templates and shadow masks to create more sophisticated surface patterns,[5,6] with applications as photonic,[28] phononic,[29,30] and plasmonic materials,[31–33] anti-reflective,[34] transparent-conductive,[35] and self-cleaning coatings,[36] light-management layers in solar cells,[37] or as substrates to control cell–surface interactions.[38,39]

Even though colloidal self-assembly is praised for its simplicity and the ability to pattern large areas, the emergence of defects, small grain sizes, and irregularities in a colloidal monolayer can compromise its structure and the resultant functionalities in different ways. First, high structural regularity and long-range order are of key importance for the structure formation process itself, especially when complex assembly phases are targeted. Complex structural arrangements, such as Moiré patterns, honeycombs, or fishbone structures can arise from the controlled stacking of two monolayers with hexagonal symmetry,[22,23,40] and are easily compromised if one of the layers contains defects. Similarly, defined uniaxial deformations of a monolayer can produce Bravais lattices with square, rectangular, or chain-like symmetries,[41] but only with a well-ordered

J. Menath, R. Mohammadi, M. Böhm, N. Vogel
Institute of Particle Technology
Friedrich-Alexander University Erlangen-Nürnberg
Cauerstrasse 4, 91058 Erlangen, Germany
E-mail: nicolas.vogel@fau.de
J. C. Grauer, C. Deters, H. Löwen
Institute for Theoretical Physics II: Soft Matter
Heinrich-Heine University Düsseldorf
D-40225 Düsseldorf, Germany
B. Liebchen
Institute of Physics: Theory of Soft Matter
Technical University of Darmstadt
Hochschulstraße 12, 64289 Darmstadt, Germany
L. M. C. Janssen
Soft Matter and Biological Physics
Department of Applied Physics
Eindhoven University of Technology
Eindhoven 5600 MB, The Netherlands
The ORCID identification number(s) for the author(s) of this article can be found under https://doi.org/10.1002/adma.202206593.

DOI: 10.1002/adma.202206593

hexagonal monolayer as a starting point. Second, the conversion of a colloidal monolayer template into functional nanostructures can be very sensitive to defects and irregularities. Complex plasmonic nanostructures, which are created by multiple, angle-dependent metal evaporation steps through a colloidal monolayer mask can only form in a reproducible fashion if the local interstitial structure and global orientation of the monolayer is constant throughout the area of interest.[31,33,42–45] Similarly, silicon nanowire arrays prepared by chemical etching of substrates patterned by a colloidal monolayer can exhibit remarkable accuracy and complexity[46–48] only with homogenous etching conditions provided by an essentially defect-free colloidal template.[49] Third, the emergent functional property of the surface pattern can necessitate colloidal assemblies with long-range order. This requirement is most critical for collective phenomena such as plasmonic surface lattice resonances, which are only observed in ordered lattices and are very sensitive to defects and irregularities.[43,50,51] Photonic crystals, prepared by stacking individual layers, similarly require ordered monolayers for accurate performance.[28,52,53]

While formation processes of colloidal monolayers from a variety of different building blocks are well established,[10,11] methods to systematically improve crystal quality are still in their infancy. In an interfacial colloidal assembly, the interplay between attractive capillary and van-der-Waals forces and repulsive electrostatic forces governs particle interactions and self-assembly.[15] At an air/water interface, this balance usually drives monodispersed particles into a hexagonally close-packed arrangement, forming polycrystalline monolayers with grains of various sizes. Due to the attractive interactions, the system cannot spontaneously reorganize toward a lower energy state with fewer defects and larger grains. Annealing the interfacial crystal therefore requires passing through an out-of-equilibrium state by means of external stimuli, such as barrier movements in a Langmuir–Blodgett trough,[54] ultrasound modules in the water subphase,[54] vibrations of a free standing film,[55] movement of active particles through the monolayer,[56] gas flows impacting on a surfactant-modified colloidal monolayer[57] and electric fields stimulating particles within the crystal.[58]

The means by which the individual particles rearrange to anneal the crystal is a fundamental question in the annealing process. Both the movement of individual particles from one grain to another,[54] as well as collective rotations around center particles[59] have been proposed as annealing mechanisms, but the relation between these mechanisms remains poorly understood.

Here, we introduce a simple and generic method to efficiently anneal 2D colloidal crystals of various materials and dimensions at liquid interfaces. In particular, inspired from a conceptually similar approach to enhance the quality of 3D colloidal crystals,[60] we use acoustic stimuli provided by a conventional loudspeaker placed underneath the container holding the water subphase. In this process, the available interfacial area is dynamically expanded, so that individual particles can move and reorient. This acoustic crystallization of 2D crystals (ACDC) of colloidal particles operates by setting the air/water interface into periodic motion via standing waves. We connect the acoustic conditions in terms of the required frequency and amplitude with the surface coverage and interaction potentials of the individual particles to find robust operation conditions for the annealing process. We also introduce a minimal model and perform computer simulations which reproduce the experimental findings and show the generic nature of the process. By tracking the motion of all involved particles, the simulations further allow us to unveil the mechanism underlying the annealing process. We find that different motion patterns dominate at different length scales, ranging from the localized rearrangement of individual particles to heal out vacancies and point defects, to consecutive large-scale rotations of the particles around fixed centers to realign individual grains.

2. Results

2.1. Characterization of Order in 2D Colloidal Crystals

Quantification of the order in the colloidal monolayer is the key to assess the efficiency of the acoustic annealing process. This is especially challenging if the annealed monolayer exhibits long-range order over macroscopic dimensions or consists of small colloidal particles with nanoscale dimensions, as both aspects prevent a direct observation via optical microscopy. To overcome this challenge, we take advantage of structural coloration arising from the periodic arrangement of the particles within the 2D colloidal crystal.[61] This method allows assessing order and grain boundaries in the square centimeter range, even for nanoscale particles. For this optical characterization, we transfer the interfacial colloidal monolayer to a solid substrate and use a customized microscopy setup to illuminate the sample with monochromatic, collimated light ($\lambda = 470$ nm) under varying angles of incidence (**Figure 1**a,b). As the individual crystal grains exhibit different lattice orientations, illumination at a given angle only produces structural coloration in grains with matching orientation, as schematically illustrated in Figure 1a. Rotating the incidence angle thus detects different crystal grains separately.

We exemplarily demonstrate the procedure using a colloidal monolayer consisting of polystyrene (PS) particles with diameter $d = 1$ µm, assembled by spreading a colloidal dispersion with 50 vol% ethanol to the air/water interface of a beaker and subsequently transferring it to a microscope slide.[27] Figure 1d–g shows microscopy images of the illuminated samples under different illumination conditions, with the angle of incidence varying between −15° and 30° in a stepwise manner. Due to the hexagonal crystal symmetry, this range of angles probes the complete sample, as is evident from the combined image of all angles, shown in Figure 1c (grains are marked in different color to facilitate grain distinction). The optical microscopy images can then be post-processed and binarized to quantify the grain sizes (details in Experimental Section). Figure 1h exemplarily shows the 30 largest grains of the prepared monolayer, detected by the structural color-based evaluation, which we term light incidence-angle analysis (LIA).

We next verify the LIA method by a direct image analysis, which is possible due to the comparably large size of the individual particles (Figure 1i–l). We use a 100× objective lens, where individual particles are resolved, as seen in Figure 1l.

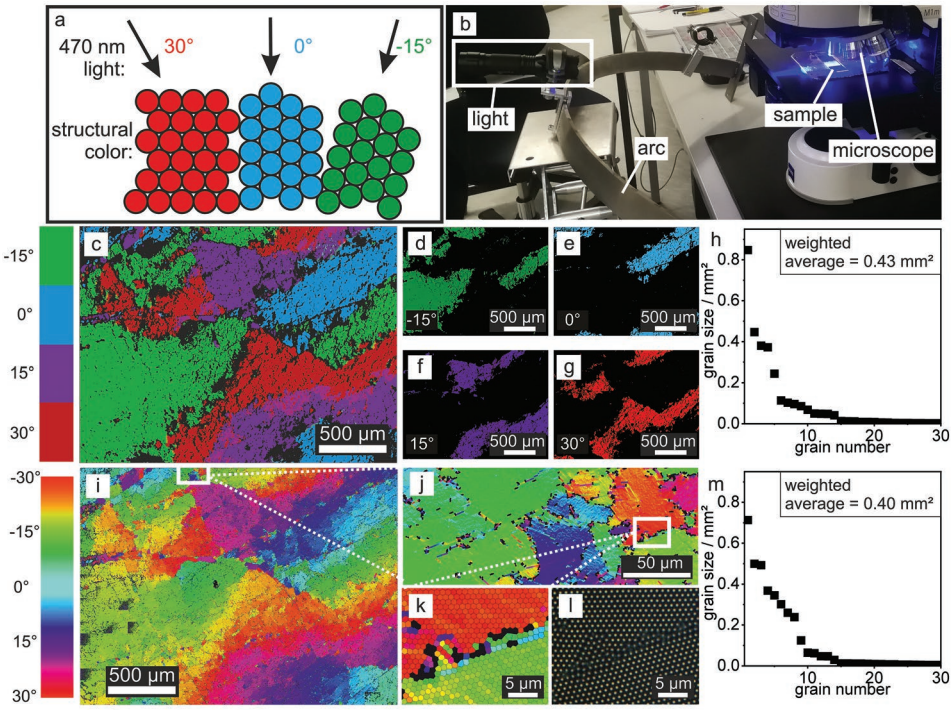

Figure 1. Evaluation of grain sizes in a colloidal monolayer based on angle-dependent structural coloration. a) Schematic illustration of three adjacent grains which are illuminated with monochromatic light from different incidence angles. Color is only observed if the lattice orientation matches the angle of light incidence, allowing for distinction between individual grains. Note that the different hue in the cartoon is only for illustration purposes; In the experiment, the grains will have the same color, but appear at different light incidence angles. b) Setup for the light incidence angle analysis (LIA). A colloidal monolayer transferred to a solid substrate is illuminated in an optical microscope with collimated light at different incidence angles. The light source is mounted externally to an arc and can be positioned at predefined locations. The light source then illuminates the sample, which is observed through the optical microscope. c–h) Characterization of grain structure and order via the LIA method. c) Composite of four microscopy images taken at different incidence angles, which are represented by false colors to distinguish the different grains. d–g) Individual 5× images, showing different grains from illumination at different incidence angles recorded in reflection mode. h) Statistical evaluation of the size of the 30 largest grains determined by image analysis from the LIA image. i–m) Verification of the method from rigorous tracking of individual particles from high-magnification images. i) Composite image consisting of 400 individual 100× microscopy images, analyzed by tracking every individual particle and color coding the phase angle of its lattice position. j) Section of (i) consisting of two 100× microscopy images. k) Smaller color-coded section of (j), highlighting the tracking of individual particles and the accurate determination of grain orientation and grain boundary from the image analysis. l) Raw image of (k) recorded in the microscope. m) Statistical evaluation of the size of the 30 largest grains determined by particle tracking.

The particles can be tracked using a custom-written Matlab software, and the order can be analyzed by color-coding the Voronoi cells of the particles according to the phase angle of the lattice. Hence, individual grains and grain boundaries can be directly visualized (Figure 1k). We then combine individual high-resolution images to capture larger areas and thus the grain structure of the monolayer (Figure 1i,j). A total area of 4.2 mm^2, which is equal to that of the single structural color image taken with a 5× objective lens (Figure 1c), can thus be precisely analyzed at the single-particle level by stitching together 400 high-magnification microscopy images (Figure 1i). All large crystal grains detected in the rigorous, single-particle tracking method are also found in the LIA image (Figure 1h,m). From LIA, we determine a weighted average area of grain A_g = 0.43 mm^2, which is close to the value obtained by direct analysis (A_g = 0.40 mm^2) and indicates that the coarse-grained color-based method correctly captures the majority of the particles. This comparison demonstrates that the LIA affords a comparably simple, large area quantification of crystal structure and order, which is the subject of this study.

2.2. Acoustic Annealing

Next, we demonstrate the ACDC process to improve the long-range order of the interfacial colloidal monolayer. The process capitalizes on the global expansion of the available interfacial area, which enables particle movement and thus a transition into a new equilibrium structure. To control the interfacial area, we devise a simple setup that uses a loudspeaker to create standing waves at the air/water interface (**Figure 2**a). The interfacial monolayer is prepared by spreading an ethanolic dispersion of PS colloidal particles (d = 1 µm) to the interface (Movie S1, Supporting Information), following established protocols.[26,27] We statistically analyze the formed monolayer after transfer to a solid substrate, shown in Figure 2c, using the LIA method and determine an average grain size A_g = 2.0 mm^2. We subsequently use the ACDC process with a fixed interfacial coverage of 88% and a frequency of 4 Hz. The annealing efficiency is very sensitive to the amplitude of the acoustic wave, which is controlled by the applied voltage. Movie S1 in the Supporting Information shows an amplitude sweep with increasing

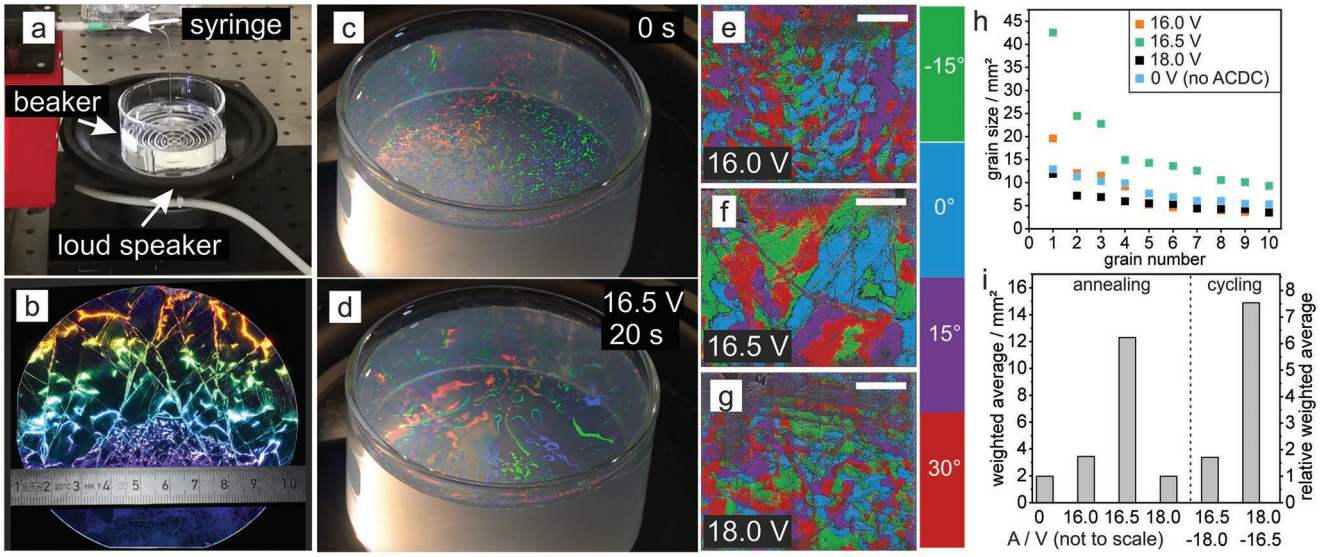

Figure 2. Acoustic crystallization of 2D crystals (ACDC) of colloidal particles as a function of applied amplitude. a) Experimental setup for the ACDC process consisting of a loudspeaker with a round beaker on top. The syringe pump used for the particle deposition to the air/water interface can be seen on the left. In the experiments, a colloidal monolayer with a surface coverage of 88% and a frequency $f = 4$ Hz was used. b) Transfer of the interfacial colloidal monolayer to a silicon wafer substrate, demonstrating the large grains after annealing. c,d) Photographs of the interfacial colloidal monolayer before and after the ACDC process. e–g) Superimposed LIA images of the individual, angle-dependent microscopy color images of a deposited colloidal monolayer's annealed amplitudes of 16.0, 16.5, and 18.0 V, respectively. h) Statistical evaluation of the size of the ten largest grains for the different amplitudes. i) Average grain sizes as a function of the annealing amplitude (left four bars), and during periodic cycling between different amplitudes (right two bars). In this case, a sample annealed at 16.5 V was subjected to 18.0 V, which reduced the crystal size (left bar). If this sample was re-annealed at 16.5 V (right bar), the well-ordered state with large average grain sizes was recovered. All scale bars: 5 mm.

voltage. Only after a sufficient amplitude is reached (in the example, 16.5 V), visible particle rearrangements into larger grains are observed. Further increasing the applied voltage, however, is detrimental for the annealing and leads to decreased order as the interface is too violently disturbed (Figure 2i, 18 V). Noteworthily, the effect is reversible and changing the applied voltage produces cyclic transitions between states of high and low order in the interfacial monolayer (Figure 2i, 18 to 16.5 V). At even higher amplitudes of 20 V, the monolayer is irreversibly damaged and largely removed from the interface as the interfacial motion becomes violent and droplets start to form and splash (Figure S1, Supporting Information). Note that this frequency-dependence of the annealing process for the interfacial colloidal monolayer is qualitatively different from the acoustic annealing of 3D colloidal crystals, which can be performed using white noise with a broadband frequency.[60]

The interfacial colloidal monolayer after annealing for 20 s with the optimized amplitude of 16.5 V is shown in Figure 2d. The increased order with cm-scale crystal grains is directly seen from its structural coloration. The same monolayer can be manually transferred to a silicon wafer substrate, highlighting the ability to produce wafer scale surface structures with macroscopic crystal orientation (Figure 2b). Note that for the deposition on a solid substrate, the interface needs to be jammed by spreading of additional particles to avoid rearrangement and loss of order during transfer and drying.

We quantify the amplitude-dependent annealing using the LIA method after transferring the samples to a solid substrate. Figure 2e–g shows the superimposed images of four microscopy images taken at different light incidence angles of the annealed monolayers for the different amplitudes. Each image covers an area of 3.8 cm^2 and is stitched together from 90 images at 5× magnification. The size of the ten largest crystal grains detected from image analysis, shown in Figure 2h, shows the global increase in grain sizes for the annealing at 16.5 V, and the destruction of order for the higher amplitude of 18 V, corroborating the visual impression of the interfacial monolayer. With an optimized amplitude, the average grain size in the 2D crystal grows to 12.3 mm^2 (Figure 2i), constituting a reproducible increase in order by more than six times compared to the reference (Figures S2 and S3, Supporting Information). The annealing frequency can be similarly used to cycle between ordered and disordered states of the monolayer (Movie S2, Supporting Information). Note that amplitude and frequency are coupled and need to be jointly optimized for efficient annealing (Figure S4, Supporting Information). The optimal amplitude and frequency are not universal properties of the process, but serve to induce standing waves at the air/water interface, and therefore change with other experimental parameters, such as the size of the speaker and the size and mass of the water-filled beaker. In the example, using frequency/amplitude combinations that support circular surface waves with a wavelength of ≈1 cm leads to annealing of the interfacial crystal, while instable surface wave patterns caused by increased frequency or amplitude are detrimental for the annealing. In practice, optimal conditions can be easily found by observing the evolution of color directly at the air/water interface while tuning the parameters individually (Supporting Information—guide to experimentalists). In fact, the system is sufficiently robust that simply playing music via the speaker with adjusted volume allows for an efficient ACDC process, as demonstrated in Movie S3 in the Supporting Information.

Even a wine glass can be used to anneal colloidal crystals by stroking the rim, setting in motion the water within (Movie S4, Supporting Information).

2.3. Influence of Surface Coverage and Interparticle Distance

Next, we discuss the influence of the surface coverage on the annealing process. When the colloidal dispersion is added to the air/water interface, ethanol is typically used as a spreading agent to increase the number of particles adsorbed to the interface. The resultant Marangoni flow pushes the particles radially outward, opening a hole in the formed interfacial monolayer at the contact point of the dispersion with the air/water interface (**Figure 3**a and Movie S1, Supporting Information). We define the surface coverage η as the fraction of the complete interfacial area of the beaker that is visibly covered by particles during the deposition process (i.e., excluding the dimensions of the hole in the monolayer upon spreading). During addition of the colloidal dispersion, the size of the hole decreases, η increases, and reaches 100% when the interface is fully covered. Note that this definition of η only indicates the fraction of the interface covered with a particle layer, as extracted from images during spreading. It ignores the fact that a perfect, hexagonally close-packed monolayer only covers 91% of the interface. Importantly, when the addition is stopped with surface coverages between $50\% < \eta < 100\%$, the hole rapidly closes as the interfacial particles relax to find their equilibrium positions (Movie S1, Supporting Information). The efficiency of the ACDC process shows an optimum for intermediate values of η (Figure 3). Annealing of a fully covered interface ($\eta \approx 100\%$) is inefficient and does not improve the order. In contrast, the order of the annealed monolayer is significantly increased for $\eta = 77 - 88\%$, while lower surface coverages ($\eta = 52\%$) reduce the annealing efficiency again.

To understand this phenomenon, we investigate the surface coverage-dependent interparticle distance within the colloidal monolayer at the air/water interface. The closing of the hole upon equilibration after spreading indicates that the particle interactions are dominated by repulsive effects, at least for $\eta > 50\%$, which is surprising as it is generally assumed that at the air/water interface attractive interactions dominate.[15,62,63] We directly measure the average interparticle distance of the particles within the colloidal monolayer at the air/water interface, d_{ip}, using laser diffraction.[64] We illuminate the colloidal monolayer with a green laser (λ = 532 nm) under normal incidence and calculate d_{ip} from the distance r of the diffraction peaks recorded in transmission at a distance L (Figure S5, Supporting Information) using[64]

$$d_{ip} = \frac{\lambda}{r/\left(L^2 + r^2\right)^{1/2}} \tag{1}$$

Figure 4a shows the evolution of interparticle distances as the system undergoes several spreading and equilibration steps until the interface is fully covered. Representative images of the interfacial monolayer and diffraction patterns at different steps of the monolayer formation process are shown in Figure 4b,c. Movies S5 and S6 in the Supporting Information show the complete evolution of the monolayer structure and the diffraction patterns, respectively. The periodic fluctuations of the interparticle distance relate to the spreading/equilibration cycles. Whenever particle dispersion is added, the interfacial monolayer is compressed by the Marangoni flow, resulting in small interparticle distances. Once the addition is stopped, the interparticle distance increases as the particles equilibrate

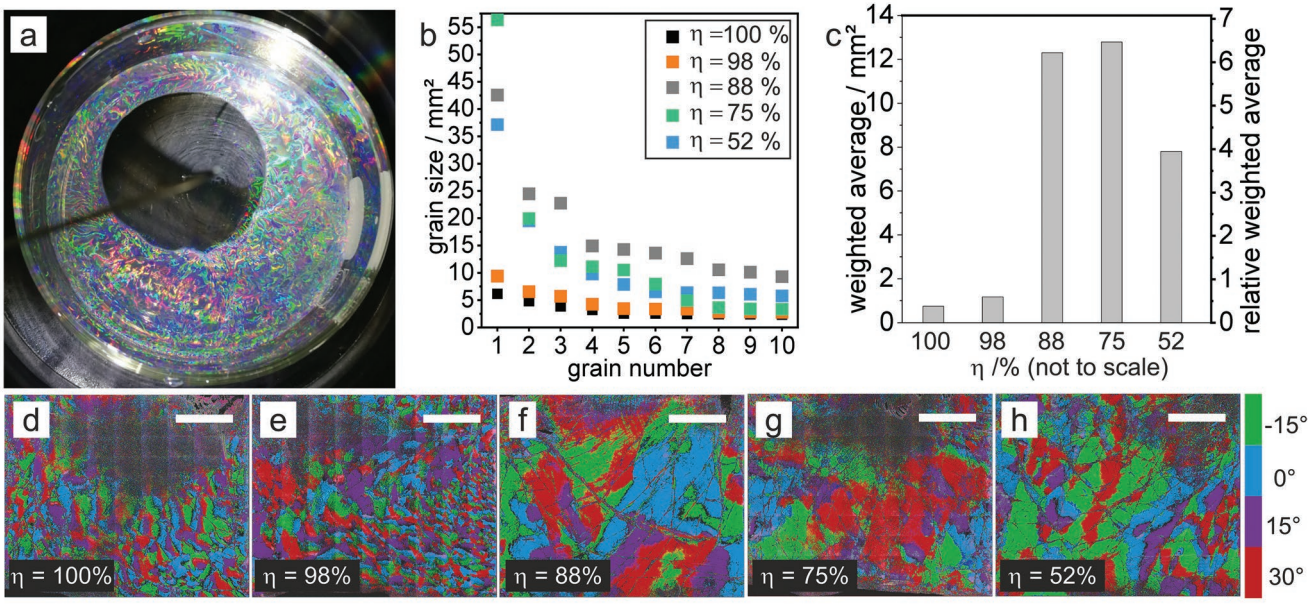

Figure 3. Efficiency of the ACDC process as a function of the interfacial surface coverage with the colloidal monolayer. a) Image of the interfacial monolayer upon formation by spreading an ethanolic colloidal dispersion. Marangoni-flows generate an outward movement and induce a hole at the contact point. b) Size of the ten largest grains at different surface coverages after the ACDC process. c) Average grain size at different surface coverages after the ACDC process. d–h) Superimposed LIA images after annealing. All experiments were performed with A = 16.5 V, f = 4 Hz, t = 1 min. Scale bar: 5 mm.

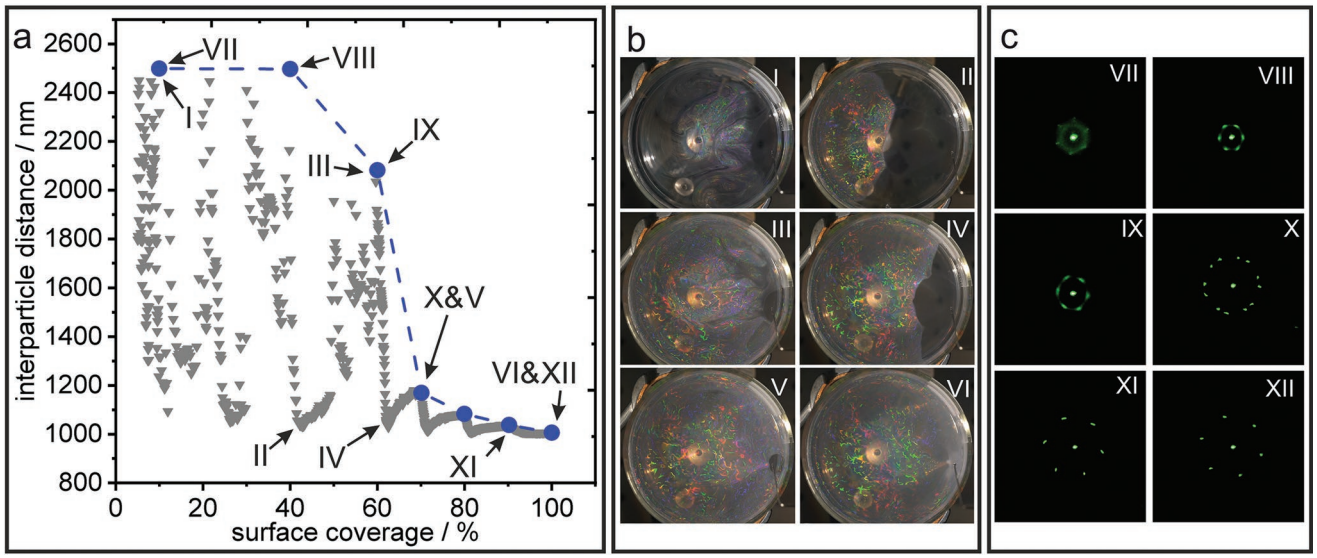

Figure 4. Interparticle distances within the interfacial colloidal monolayer. a) Interparticle distance as a function of surface coverage, measured by laser diffraction. Equilibrium distances are marked in blue, out-of-equilibrium distances during spreading and reorganization are marked in gray. b) Representative photographs of the interfacial colloidal monolayer at different surfaces coverages marked in (a). c) Photographs of the diffraction patterns from a laser transmitted though the interfacial monolayer at representative surface coverages indicated in (a), used to determine the interparticle distances.

(see, e.g., Figure 4, images II,III and IV,V). For $\eta <$ ≈50% isolated patches with persistent structural color are observed (Figure 4, image I). This behavior indicates the presence of weak attractive interactions that are sufficient to induce the formation of ordered monolayer patches but do not cause irreversible agglomeration as the particles can be compressed and relaxed upon further addition steps. We measure a constant interparticle distance $d \approx 2500$ nm within the equilibrated patches, regardless of the surface coverage, which suggests the presence of a secondary attractive minimum in the interaction potential at this comparably large interparticle distance (the particle diameter is 1 µm), presumably caused by capillary forces.[15,62,63] For $\eta >$ ≈75% the equilibrated monolayer covers the entire interface (Figure 4V,VI). Concurrently, the measured interparticle distance continuously decreases with increasing surface coverage (Figure 4, IX–XII), suggesting a dominant repulsive interaction, where the system cannot fully equilibrate into the energetic minimum at $d \approx 2500$ nm. When the interface is completely covered and no more particles can be added ($\eta = 100\%$), the measured average distance is $d \approx 1050$ nm, which is close to the particle's diameter. Note that the individual particles retain their mobility, seen by an equilibration to larger interparticle distances if parts of the interfacial monolayer are removed (Movie S7, Supporting Information). Adding salt to the subphase after formation of the interfacial monolayer decreases the interparticle distance until the system forms a close-packed monolayer with interparticle distances close to the particle diameter ($c_{NaCl} \approx (10\ \text{mmol})/L$; Figure S6, Supporting Information) and the particles remain fixed in this position without re-equilibration, even for comparatively low initial surface coverages (Movie S8, Supporting Information). This behavior suggests that electrostatic repulsion is responsible for particle separation and rearrangement. When the charges are screened, the particles are irreversibly trapped in a primary energetic minimum. Note that this salt addition after assembly and annealing constitutes a simple means to fix the particle positions within the ordered monolayer and facilitates the deposition to a solid substrate without risking a rearrangement of the particles and loss of order during the transfer. In contrast, the direct addition to a salt-containing subphase does not produce an ordered interfacial structure as the particles agglomerate rapidly without ordering (Movie S8, Supporting Information). When particles are removed from a salt-containing subphase, the monolayer does not re-equilibrate, confirming the loss of repulsive interactions (Movie S9, Supporting Information).

We can now rationalize the dependence of the ACDC process on the interfacial structure of the monolayer shown in Figure 3. For an efficient annealing process, the particles need to be sufficiently separated to enable rearrangement into a lower energy configuration with fewer defects. At large surface coverages, the particles are too close to enable such rearrangements even with the additional surface area generated via the acoustic vibrations. At intermediate surface coverages ($77\% < \eta < 88\%$), the mutual repulsion opens up sufficient interfacial space to enable particle rearrangement. At an even lower surface coverage, the interface is not yet fully covered and the individual particles do not show significant repulsive interactions, which is why providing additional interface in the ACDC process is less efficient in this case.

2.4. Simulations of the ACDC Process and Mechanism of Annealing

Building on the experimental investigations, we devise a theoretical model to investigate the ACDC process in simulations. The model assumes a polycrystalline 2D crystal with repulsive

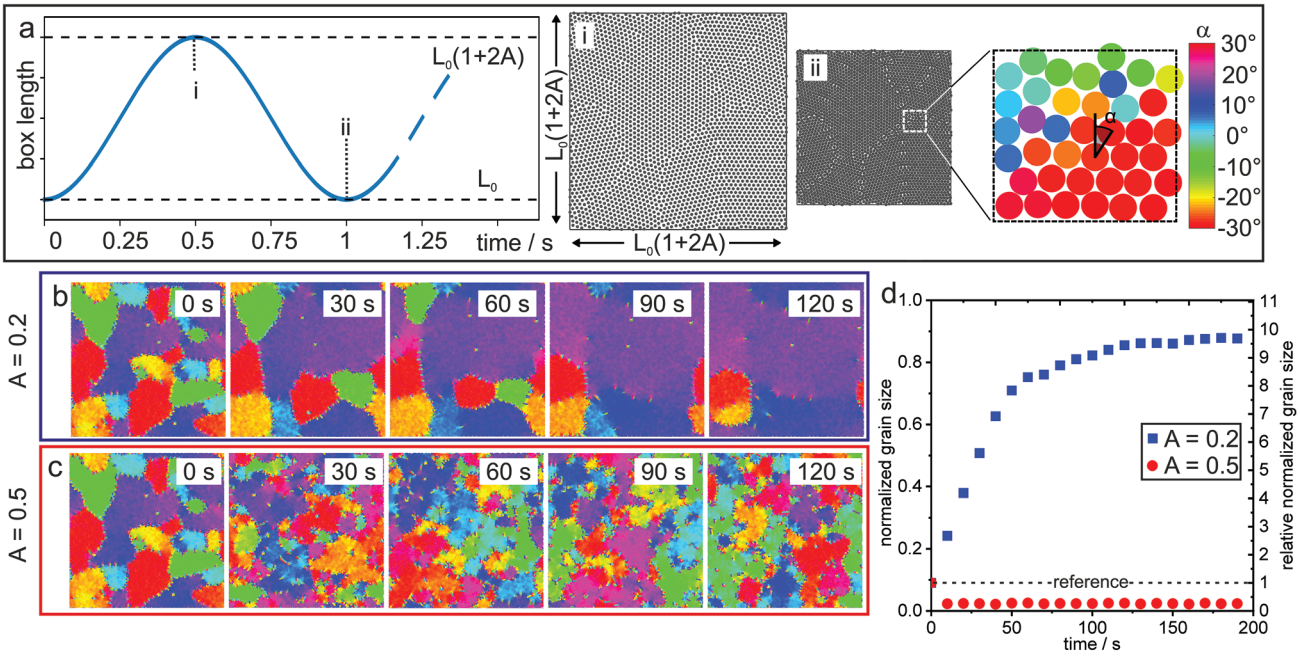

Figure 5. Simulations of the annealing process based on a cyclic expansion of a box filled with repulsive particles. a) Evolution of the dimensions of the simulation box over time, shown for a frequency of 1 Hz and an amplitude *A*. i,ii) The 2D crystal within the box undergoes periodic expansion and compression. Coloration of the phase angle of the individual particles allows detection of different grains. b,c) Evolution of grain sizes for the annealing process at two exemplary amplitudes $A = 0.2$ (b) and $A = 0.5$ (c), using $\eta = 74\%$ and $f = 1$ Hz. d) Statistical evaluation of the average grain sizes in the course of the annealing process.

interactions modeled by a Yukawa pair potential (details in the Experimental Section). The expansion of the air/water interface in experiments is mimicked by a cyclic affine expansion of the square simulation box (**Figure 5**a), where the initial length L_0 is periodically expanded to a length of $L_0(1 + 2A)$ given by the amplitude *A*. Figure 5b,c shows the evolution of the grain structure of the 2D crystal upon annealing with different amplitudes, while keeping the frequency at 1 Hz. Using $A = 0.2$, the grains continuously grow, reaching, within a few minutes, an increase in average grain size by a factor of 9.7 as compared to the nondriven case (Figure 5d). When the amplitude is changed to $A = 0.5$, however, the annealing process fails and the order is decreased, evidenced by a reduction in grain size to 26% of the reference ($A = 0$). Both trends qualitatively reproduce the experimental results shown in Figure 2.

We use the simulations to systematically explore the parameter space. **Figure 6**a shows the dependence of the grain size on the driving amplitude, keeping all other parameters constant. With increasing amplitude, the efficiency of the annealing increases, goes through a maximum, and then rapidly decreases until defects are induced and individual grains break up, leading to a reduction of order. A similar behavior results from a variation in annealing frequency using a fixed amplitude (Figure 6b). Indeed, with increasing frequency, particle re-organization is first facilitated and the average grain size steeply increases until the annealing is most efficient. A

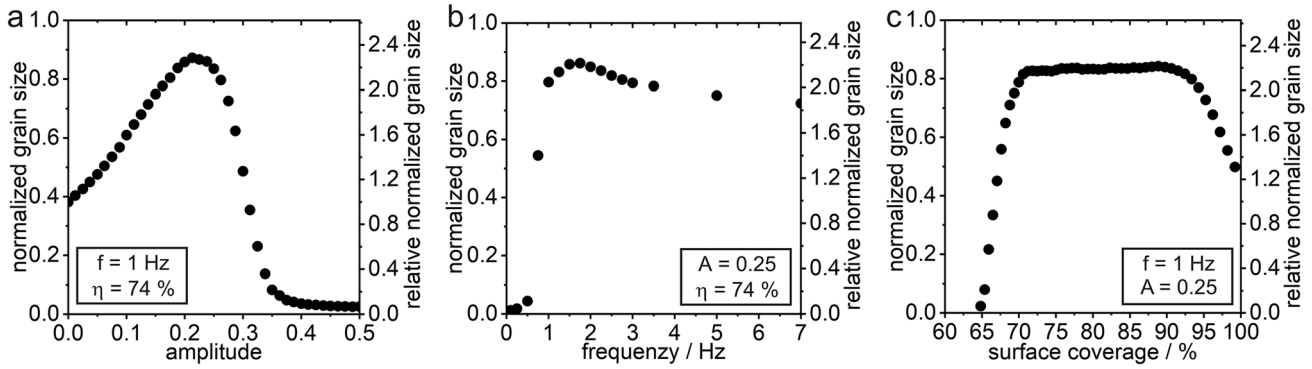

Figure 6. Simulated annealing process as a function of relevant process parameters. a) Influence of amplitude, b) frequency, and c) surface coverage on the normalized and relative normalized grain size.

further increase in frequency causes a slight reduction in grain sizes as the particles cannot re-organize sufficiently fast. The simulations also predict an optimal window for the surface coverage of the particles (Figure 6c), which qualitatively reproduced the optimal range determined in experiment (Figure 3). Similar to the experimental case, we define $\eta = 100\%$ as a complete hexagonally close-packed particle layer. The grain size can be efficiently increased using surface coverages between $70\% < \eta < 95\%$, while both larger and smaller values of η prevent efficient annealing. Note that quantitative difference between simulation and experiments may be caused by the drastically different system size and the difference in assumed interaction potential between the particles.[60] A simple scaling analysis connecting the time-dependent evolution of the energy barrier that needs to be overcome to enable annealing qualitative corroborates with the optimal frequency and amplitude found for the given particle system (details in Supporting Information and Figure S7, Supporting Information).

The parameter study of this simplified simulation model, and the qualitative agreement with the experimental results suggests the following mechanism. The ACDC process is driven by movement of repulsively interacting particles made possible by an increase in available area, which causes a local reorganization into a structure with higher order. The annealing is efficient if sufficient area is made available by choosing a suitable intermediate surface coverage and annealing amplitude. Too low amplitudes or too large surface coverages prevent a local rearrangement, while too large amplitudes and too low surface coverages favor larger-scale structural reorganizations, which lead to new defects and disintegrate the crystalline structure. Note that this simplified model does not take into account the pattern of the surface waves created at the liquid interface. Modal engineering of such surface waves into complex patterns,[65] e.g., in the form of Rayleigh waves,[66] has been used to direct the formation of defined patterns of (individual) microparticles,[67] liquid crystalline molecules,[68] or bacterial biofilms,[69] and may thus provide an interesting opportunity to further influence and potentially control the annealing process.

We now turn to the microscopic mechanism of grain annealing by studying the movement of individual particles in our simulations. **Figure 7** displays simulation snapshots during and after annealing of a defect structure (right columns), taken from Movies S10–S13 in the Supporting Information, along with the complete trajectories of all particles (left column). Two distinct mechanisms collude to anneal

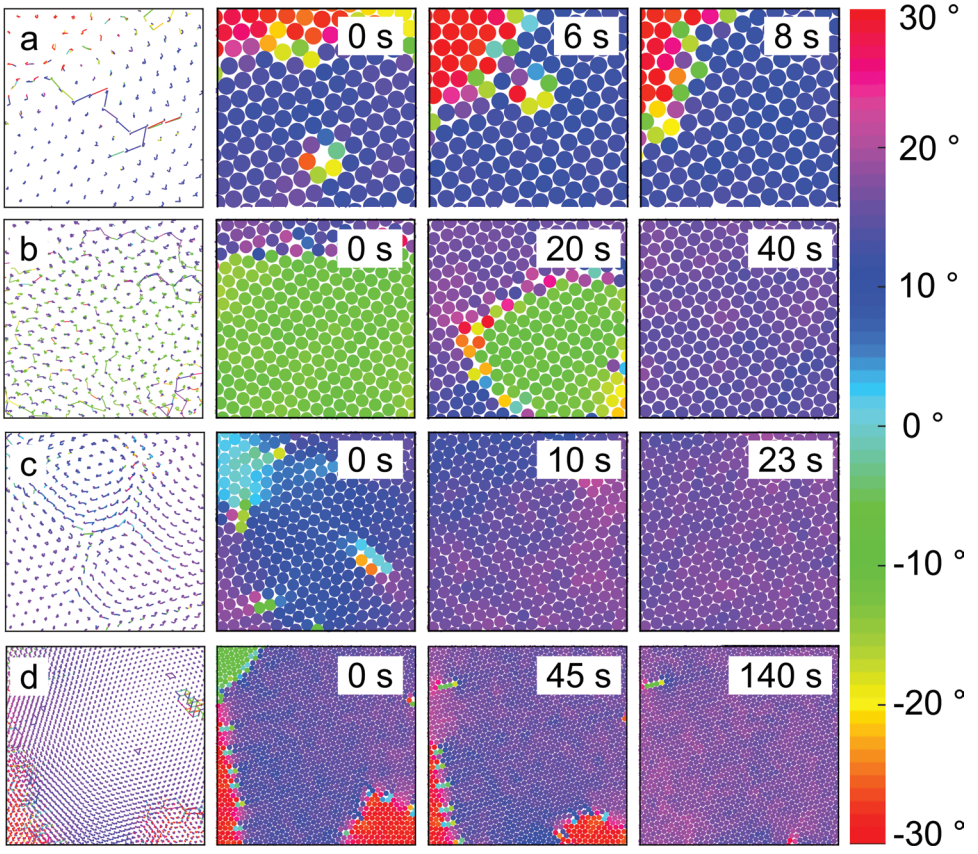

Figure 7. Mechanistic investigation of the annealing process showing characteristic rearrangement movements at different length scales. The figure shows the full particle trajectories (left) and exemplary snapshots of the 2D crystal at different time points (right). a) At the smallest length scale, individual point defects are annealed by local arrangements between neighboring particles. b–d) Granule formation as the dominating microscopic annealing mechanism. Larger-scale rotations around center particles align different grains. The size of the rotations depends on the orientation angle mismatch, shown for 30° (b), 10° (c), and 5° (d).

defects at different length scales. Point defects, such as vacancies, are efficiently annealed by the individual movement of neighboring particles that move the defect toward a grain boundary (Figure 7a and Movie S10, Supporting Information). The dominating mechanism to increase order at larger scales, both in simulation and experiments is the merging of complete grains to remove grain boundaries. This merging occurs by transfer of individual particles from one grain to another, in agreement with literature.[54] Noteworthily, the complete particle trajectories during the annealing reveal larger-scale patterns with hexagonal symmetry (Figure 7, left), which evidence an underlying collective reorganization. These patterns coincide with motion patterns in rotating granules, an annealing mechanism only recently reported by Barth et al.[59] In this mechanism, a grain splits up into smaller cells, termed granules, that each rotate around a center particle to locally reorient the particles within the individual granule. The center particles do not need to move during annealing, as they are in phase with the lattices of both neighboring grains. Collectively, the counterrotation of all involved granules causes a larger-scale reorientation of the entire grain to match the lattice of the neighboring grain. The particle trajectories exhibit characteristic structural motifs resulting from the Moiré pattern formed by the superposition of the lattices of both grains. In contrast to the system of Barth et al., these collective granule movements in our periodically expanding system do not occur simultaneously, but via successive granule alignment.

An analysis of the collective movement visualized in the particle trajectories during annealing of grain boundaries between grains with different orientation angles further supports this mechanism (Figure 7b–d). For a large orientation angle mismatch of 30°, we observe small hexagonal patterns formed by nearest neighbors moving around a center particle (Figure 7b and Movie S11, Supporting Information). With an orientation angle mismatch of 10°, the scale of the hexagonal domain increases and more particles move in a collective pattern for grain alignment (Figure 7c and Movie S12, Supporting Information). At smallest orientation angle mismatch of 5°, the motion pattern nearly covers the entire grain, indicating a collective rotation of many particles by small amounts to merge with the neighboring grain (Figure 7d and Movie S13, Supporting Information). These patterns coincide with the increase in granule dimension with decreasing orientation angle mismatch predicted for granule rotation.[59] Finally, it is noteworthy that a scaling analysis by Barth et al. shows that the energy barrier associated with granule rotation becomes rapidly prohibitive at larger grain sizes and orientation angles.[59] In contrast, our results indicate that successive granule realignment can occur at larger system sizes and for large orientation angle mismatches (i.e., forming small granules), likely because of the increase in available area during annealing.

2.5. Application of the ACDC Process to More Complex Particle Systems

Having established the involved physics via the comparably simple PS model particles, we now demonstrate the applicability of the ACDC process to more complex particles. We choose poly(*N*-isopropylacrylamide) microgels (d_h(20 °C) = 525 nm)[70] and core–shell particles consisting of a silica core and a poly(dimethylaminoethyl methacrylate) (SiO_2@PDMAEMA)[20] (d_{core} = 170 nm, $d_{h(core-shell)}$ = 360 nm). These soft particles deform under the influence of surface tension and exhibit a complex interfacial morphology (**Figure 8**a,b). Therefore, such particles have emerged as both important model systems to fundamentally investigate structure-dependent interfacial properties[22,71,72] and phase behavior,[19,20] and to produce tailored, functional surface nanostructure arrays.[43,51,73] For these experiments, we slightly modified the ACDC process, using a larger beaker and speaker, which changed the voltage/frequency conditions required for optimized annealing (Figure S8, Supporting Information).

Figure 8c,d shows high-magnification scanning electron microscopy (SEM) images of both types of particles, highlighting the non-close-packed lattice, which results from the steric repulsion between dangling chains of the soft particle shells.[20,74] As detailed above, efficient annealing occurs at the intermediate regime where the particles are mutually repulsive, yet sufficiently apart to enable rearrangement. For the soft particles, we use the surface pressure Π as a means to characterize

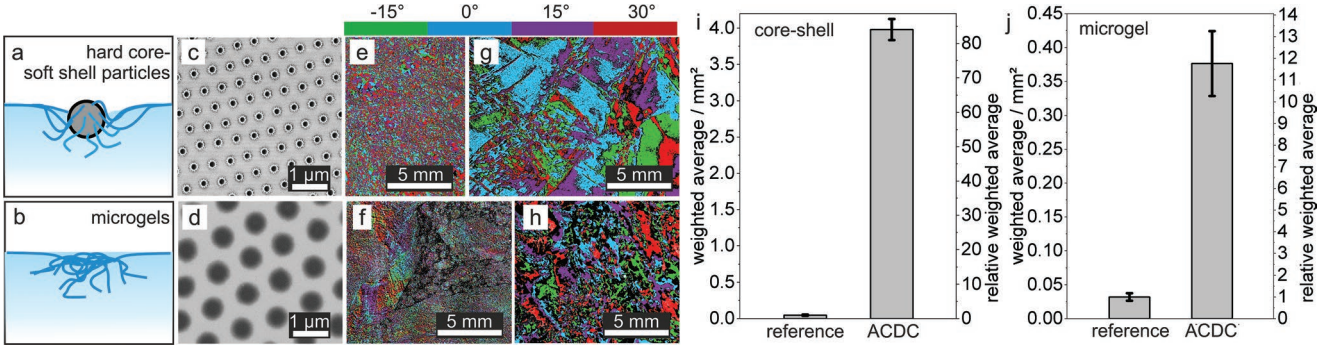

Figure 8. ACDC process for soft particle systems. a,b) Schematic representation of the morphology of a hard core–soft shell particle (a) and a microgel at the air/water interface (b). c,d) SEM images of interfacial monolayers of core–shell particles (c) and microgels monolayer (d) deposited on a silicon wafer. e–h) LIA-composite images of the core–shell particle monolayer (top row) and the microgel monolayer (bottom row) before (e,f) and after (g,h) the ACDC process. i,j) Average grain sizes for core–shell particles (i) and microgels (j) before and after the ACDC process. All experiments were performed with A = 0.18 V, f = 30 Hz, t = 120 s.

the surface coverage[20,70] and available interfacial area per particle, and determine optimal conditions at Π = 3–5 mN m^{-1}. Figure 8e,f shows the superimposed LIA images of the interfacial monolayers after transfer to a silicon wafer substrate, for the core–shell particles and microgels, respectively. The successful annealing process can be readily seen by the superimposed LIA images of both systems after acoustic annealing at 30 Hz and 0.18 V for 120 s (Figure 8g,h). Statistical evaluation of the average grain sizes reveals an increase by a factor of 84 for the core–shell particles (Figure 8i) and by a factor of 12 for the microgels (Figure 8j). Note that the application of the LIA method is more challenging for the microgel samples, because of the low refractive index contrast and less defined surface topography. The reduced coloration results in incomplete imaging of the grain structure, as evidenced from the black parts in the compound images in Figure 8f,h, and therefore likely underestimates the total degree of order.

To further analyze the grain structure, we combine multiple SEM images of the particle monolayers and use image analysis to color-code the individual particles according to their phase angle (Figure S9, Supporting Information). The increase in grain size from this direct analysis method for both types of particle systems confirms the LIA results and shows that the simple light incidence angle analysis can be applied for a variety of different particle systems.

3. Conclusion

We demonstrate an experimentally simple and convenient method to anneal interfacial colloidal crystals based on the creation of standing waves induces by acoustic vibrations from a speaker. With optimized annealing conditions, formed by adjusting amplitude, frequency, and surface coverage of the particles, single crystal grains with square centimeter dimensions can be routinely produced, even with complex, deformable microgels or core–shell particles. By combining direct observations of the interparticle distance and equilibration of the colloidal particles at the interface with a simulation model, we provide a mechanistic understanding of the annealing process at both macroscopic and microscopic scales. Noteworthily, even the most simplistic setup involving a typical crystallization dish placed onto a conventional speaker allowed for efficient annealing. Improving the vibration transmission by mechanical coupling or modal engineering of the created surface waves can be readily envisioned to improve effectivity and quality of the annealed colloidal monolayer, or to engineer defined defects or grain boundaries along the modal structure at the interface. It is our hope that the simple yet efficient annealing process, paired with the fundamental insights gained in this study will spark new advances not only in the field of surface pattern production, but also in the characterization and theoretical understanding of crystallization and structure formation in soft matter.

4. Experimental Section

PS Particle Synthesis: Monodispersed PS particles synthesized by a surfactant-free emulsion polymerization were used for the monolayer formation. For the synthesis, 250 mL water was heated to 80 °C in a 500 mL triple-neck round-bottom flask and flushed with nitrogen for 30 min. As synthesis components, 80 g styrene and 0.4 g acrylic acid as comonomer, which was first dissolved in 5 mL water, were used. The addition of these two components under constant stirring was followed by 0.1 g ammonium peroxodisulfate (APS), dissolved in 5 mL water, after 5 min. The reaction at 80 °C was continued for 24 h and the dispersion was subsequently cooled down to room temperature. Purification was performed by consecutive centrifugation and redispersion steps and dialysis against water for 1 months with a daily change of water.[27] Prior monolayer formation, the dispersion was cleaned as well, as previous research in our group showed that this cleaning is significant for creating proper interfacial monolayers.[75] First, the particle suspension was mixed with 1:1 ratio ethanol (≥99.8%, Carl Roth) and centrifuged with 10 000 rpm for 3 min with the Eppendorf centrifuge 5804R. The settled particles were then redispersed in Milli-Q water (18.2 MΩ, Elga PURELAB Flex) with an ultrasonic bath (VWR ultrasonic cleaner).

Microgel Synthesis: The microgel synthesis was described in a previous study.[70] In short, 2.83 g of N-isopropylacrylamide (NiPAm) and 193 mg of N,N-'methylene(is)acrylamide (BIS) were dissolved in 249 mL of Milli-Q water in a 500 mL three-neck round bottom flask equipped with reflux condensers and stirrers. The solution was heated to 80 °C and purged with nitrogen gas. After 30 min of equilibration, 14.3 mg of APS in 1 mL of Milli-Q was added. After 5 h, the mixture was cooled to room temperature. The dispersion was purified by centrifugation and redispersion in Milli-Q water three times, followed by dialysis against Milli-Q water for 1 week.

Core–Shell Particle Synthesis: The synthesis of the core–shell particles was described in a previous study.[20] A dispersion of 0.9 g Stöber silica cores functionalized with the photoiniferter *N,N*-(diethylamino) dithiocarbamoylbenzyl(trimethyoxy)silane was dispersed in 162 mL dry dimethylformamide and mixed with 18 mL (2-dimethylaminoethyl) methacrylate in a 250 mL round-bottom flask. The dispersion was treated with ultrasound and flushed with argon four times to remove oxygen. Subsequently, the dispersion was placed in a UV crosslinker (Vilber Bio-Link 365) and irradiated with 365 nm UV light. After nine discrete time steps, 20 mL of the dispersion was removed and purified by centrifugation and redispersion ten times in EtOH, yielding 50 mL of a 0.3 wt% particle dispersion. The UV irradiation time used during this study was 40 min.

Monolayer Formation for the PS Particles: For the monolayer formation, a method was used described earlier in the group with slight modifications.[27] To spread the PS particles onto the air/water interface, the dispersion was mixed with ethanol in a 1:1 ratio. As subphase, 100 mL Milli-Q water was filled in a beaker with the diameter of 8 cm from Schott Duran. Figure 2a shows the experimental setup. The ethanol–water particle dispersion was filled in a 1 mL syringe and spread with a syringe pump (LA-120 by Landgraf Laborsysteme) at a rate of 21 µL min^{-1} directly to the air/water interface, as adopted from a procedure by Zhang et al.[26] For the annealing, a loudspeaker (Visation WS 17 E, Ø 14.8 cm) was placed under the beaker. Furthermore, a light source was installed to illuminate the monolayer on the water surface, so the ordering process could be observed during the experiments. The surface coverage was determined by the size of the hole created in the monolayer by the Marangoni flow of the ethanol during deposition, seen in Figure 3a and Movie S1 in the Supporting Information. After interrupting the particle flow and removing the needle, the hole closed immediately and the surface was completely covered with the particle monolayer. To observe the hole size during the experiments, a sheet of paper with defined concentric circles with a distance of 1 cm was placed below the beaker. The deposition process was recorded so that the exact hole size could be captured and measured with ImageJ after the deposition.

Acoustic Annealing: To set the parameters of the sound waves, a signal generator (Joy-it, JDS2915) was connected to the loudspeaker. Here, the amplitude and frequency of the sound waves could be chosen and varied. To finally produce the sound waves, both the signal generator and the loudspeaker under the beaker were connected to the sound box X-230 from Logitech. To anneal the core–shell particles and the microgels, the 50 W bass speaker bass pump 4 Ω from Sinus Line was used with two

$1 \times 2 \times 4$ cm^3 foamed PS dampeners on top. A $d = 8$ cm beaker, filled with 200 mL of Milli-Q water was used for the PS particle annealing and a $d = 9.4$ cm beaker for core–shell particle and microgel confinement.

Particle Deposition: For the PS particle deposition, glass substrate with a size of 22 mm x 22 mm was used, which were cleaned by rinsing with ethanol, followed by a mechanical cleaning using precision wipes (KIMTECH Science), followed by an additional ethanol rinsing and blow drying with a nitrogen stream. Directly before the deposition process, the glass slides were activated by a 5 min oxygen plasma treatment (Femto model, Diener Electronics). For the deposition, the interface was always fully covered by extra addition of colloidal dispersion via the syringe, to avoid particle movement during transfer. An alternative approach can be the addition of salt to the subphase to aggregate the particles in their interfacial position. For the transfer, the glass slide, held by a tweezer, was dipped vertically under the water surface and then turned, so it could be lifted up in a 45° angle to deposit the particles. Afterward, the glass slide with the deposited particles was dried vertically. To analyze the transferred monolayer, the backside of the glass substrates was rinsed with a precision wipe and ethanol to remove any particles there.

Monolayer Formation for Microgels and Core–Shell Particles: The microgels and the core–shell particles were dispersed in ethanol and water at a volume ratio of 1:1 with 0.05 and 0.015 wt%, respectively. The $d = 9.4$ cm beaker was placed on the bass speaker bass pump 4 Ω 50 W by Sinus Line with two $h = 2$ cm foamed PS dampeners in between (see Figure S7, Supporting Information). The beaker was filled with 200 mL Milli-Q water and placed below the dipper of a KSV-NIMA Langmuir–Blodgett through to which a 2×4 cm^2 silicon substrate was mounted at an angle of 45°. The silicon substrates were cleaned using ethanol and oxygen plasma treatment prior to deposition. The particles were spread dropwise using a 100 µL pipette. The surface pressure was measured with a Wilhelmy plate. After the desired surface pressure was reached, the Wilhelmy plate was removed and the acoustic annealing was initiated, as described above. After annealing, the substrate was raised to deposit the formed monolayer at a speed of 2 mm s^{-1}.

Characterization: Grain sizes were characterized by the LIA method (Figure 1b), which was validated by individual particle tracking (Figure 1i–m). Both measurements were conducted using an Axio Imager M1m microscope (Zeiss) with an integrated camera (AxioCam ICc1). Pictures were taken in a jigsaw mode, where single pictures from different positions were automatically recorded and stitched into one composite image that could cover the entire slide. A light-emitting diode-flashlight (Dask Fire), fixed on a customized hemicircular arc with an angle scale, illuminated the sample with blue light. For the LIA characterization, four images were taken at a magnification of five times of each sample, where the flashlight was fixed at the angles of –15°, 0°, 15°, and 30° on the tilted arc. On each picture, different grains were visible. The four pictures illuminated from these angles then produced a completely illuminated image of the whole sample. A custom written Matlab software analyzed the four images separately, by binarization and subsequent calculation of the grain sizes by multiplying the area of connected pixels in each image by the squared pixel size. These values from the single images could then be combined resulting in the grain size of the whole sample. For verification, one LIA image at 5× magnification (4.2 mm^2) was compared to an image composed of 400 100× magnification images, where individual particles were directly analyzed (Figure 1). For all other LIA characterizations, 90 individual images at 5× magnification were merged with an overlap of 10% in order to systematically quantify the grain size over an area of 3.8 cm^2.

Simulation: Unlike in ref. [76] where the particles were actively deformed, the available area here was changed periodically. In this simulation model, an ensemble of N overdamped colloidal particles at positions $\mathbf{r}_i$ in two spatial dimensions was considered, where $i = 1,..., N$ is the particle index. Periodic boundary conditions were used in both directions with a box length L. The particle coordinates were considered in the domain from $-L/2$ to L/2 in both directions. To describe the dynamics of the particle motion, the following Langevin equation was used

$$\dot{\mathbf{r}}_i(t) = \sqrt{2D}\eta_i(t) - \nabla_{\mathbf{r}_i} V(\mathbf{r}_1,...,\mathbf{r}_N)/\gamma \quad (2)$$

where D is the translational diffusion coefficient, γ is the Stokes friction coefficient (both assumed to be equal for all particles) and $\boldsymbol{\eta}_i$ represents unit-variance Gaussian white noise with zero mean. The potential $V(\mathbf{r}_1,..., \mathbf{r}_N)$ accounts for strong repulsions among particle pairs, which are modeled using a repulsive Yukawa pair potential

with $V(\mathbf{r}_1,..,\mathbf{r}_N) = \frac{1}{2}\sum_{i,j;i\neq j} v(\mathbf{r}_i,\mathbf{r}_j)$, where $v(\mathbf{r}_i,\mathbf{r}_j) = v_0 \frac{\exp(-\frac{r_{ij}}{\lambda})}{r_{ij}}$. Here, $r_{ij} = |\mathbf{r}_i - \mathbf{r}_j|$ is the distance between particles i and j, v_0 is the amplitude of the potential, and λ is a screening length.

To model the additional area that the particles gained due to the acoustic stimulation, the simulation box length $L(t)$ with the frequency f associated with the loudspeaker was periodically expanded and shrunk. The time-dependent box length was given by

$$L(t) = L_0(1 + A(1 - \cos(2\pi f t))) \quad (3)$$

with the minimum value of the initial box length L_0 and the maximal possible box length $L_0(1 + 2A)$ specified by the amplitude A.

The simulation protocol is as follows: for given particle positions $\mathbf{r}_i(t)$, two subsequent moves were applied within a small discrete time step Δt. In the first move, the particle positions were updated to $\mathbf{r}_i^{(1)}$, according to standard Brownian dynamics using an Euler integration scheme.[77]

Then, in a second move, these particle positions were scaled with the actual new simulation box length $L(t + \Delta t)$ as

$$\mathbf{r}_i(t + \Delta t) = \frac{L(t + \Delta t)}{L(t)} \mathbf{r}_i^{(1)}(t) \quad (4)$$

This procedure of double moves was repeated to generate particle trajectories.

In the simulations, the distance and time were measured in units of 1 µm and 1 s were measured and $D = 0.43$ µm^2 s^{-1}, $V_0/\gamma = 3 \times 10^5$ µm^3 s^{-1}, and $\lambda = 0.1$ µm were used. The time step was $\Delta t = 0.0001$ s.

Statistical Analysis: Due to the large grain sizes, an evaluation of the crystal pattern over areas in the square centimeter range had to be undertaken. This was achieved by the LIA method which captured about 3.7×10^8 1 µm PS particles in one 3.8 cm^2 image. The method was validated against a particle-resolved image analysis in Figure 1 and it calculated the area weighted grain size (A_g) according to Equation (5), where $A(i)$ is the area of grain i and n is the total number of grains. The grain areas were calculated by counting connected pixels in a binarized image using a Matlab script

$$A_g = \frac{\sum_{i=1}^{n} \sum A(i)^2}{\sum_{i=1}^{n} \sum A(i)} \quad (5)$$

In order to assess reproducibility between experimental runs, the raw monolayer and the annealed crystal were reproduced four times in Figures S2 and S3 in the Supporting Information, respectively. A relative standard deviation of 0.62 and 0.23 could be seen for these monolayers, respectively, which showed that the annealing was reproducible despite the expected fluctuations between experiments. The experiments could not resolve that the crystal annealing observed under the microscope after transfer corresponded exactly to the behavior at the liquid interface. However, as seen in Movies S2–S4 in the Supporting Information, a qualitative grain growth was visible directly at the interface as well.

Supporting Information

Supporting Information is available from the Wiley Online Library or from the author.

Acknowledgements

Roman Günther is acknowledged for providing the movie showing annealing in a wine glass. Simone Ciarella and Marcel Rey are

acknowledged for discussions. N.V. and H.L. acknowledge funding from the Deutsche Forschungsgemeinschaft (DFG) under grant number VO 1824/8-1 and LO 418/22-1, respectively.

Open access funding enabled and organized by Projekt DEAL.

Conflict of Interest

The authors declare no conflict of interest.

Data Availability Statement

The data that support the findings of this study are available from the corresponding author upon reasonable request.

Keywords

colloids, crystallization, monolayers, self-assembly, structural color

Received: July 20, 2022
Revised: October 13, 2022
Published online: December 1, 2022

[1] T. Palberg, *Curr. Opin. Colloid Interface Sci.* **1997**, *2*, 607.
[2] A. D. Dinsmore, J. C. Crocker, A. G. Yodh, *Curr. Opin. Colloid Interface Sci.* **1998**, *3*, 5.
[3] U. Gasser, *J. Phys.: Condens. Matter* **2009**, *21*, 203101.
[4] V. N. Manoharan, *Science* **2015**, *349*, 1253751.
[5] B. Ai, H. Möhwald, D. Wang, G. Zhang, *Adv. Mater. Interfaces* **2017**, *4*, 1600271.
[6] J. Zhang, Y. Li, X. Zhang, B. Yang, *Adv. Mater.* **2010**, *22*, 4249.
[7] V. Prasad, D. Semwogerere, E. R. Weeks, *J. Phys.: Condens. Matter* **2007**, *19*, 113102.
[8] A. M. Alsayed, M. F. Islam, J. Zhang, P. J. Collings, A. G. Yodh, *Science* **2005**, *309*, 1207.
[9] P. Pieranski, *Phys. Rev. Lett.* **1980**, *45*, 569.
[10] N. Vogel, C. K. Weiss, K. Landfester, *Soft Matter* **2012**, *8*, 4044.
[11] V. Lotito, T. Zambelli, *Adv. Colloid Interface Sci.* **2017**, *246*, 217.
[12] U. Gasser, C. Eisenmann, G. Maret, P. Keim, *ChemPhysChem* **2010**, *11*, 963.
[13] S. Deutschländer, P. Dillmann, G. Maret, P. Keim, *Proc. Natl. Acad. Sci. U. S. A.* **2015**, *112*, 6925.
[14] M. Grzelczak, J. Vermant, E. M. Furst, L. M. Liz-Marzan, *ACS Nano* **2010**, *4*, 3591.
[15] N. Vogel, M. Retsch, C. A. Fustin, A. Del Campo, U. Jonas, *Chem. Rev.* **2015**, *115*, 6265.
[16] J. Vialetto, M. Zanini, L. Isa, *Curr. Opin. Colloid Interface Sci.* **2022**, *58*, 101560.
[17] M. Rey, M. A. Fernandez-Rodriguez, M. Karg, L. Isa, N. Vogel, *Acc. Chem. Res.* **2020**, *53*, 414.
[18] M. Karg, A. Pich, T. Hellweg, T. Hoare, L. A. Lyon, J. J. Crassous, D. Suzuki, R. A. Gumerov, S. Schneider, I. I. Potemkin, W. Richtering, *Langmuir* **2019**, *35*, 6231.
[19] M. A. Fernandez-Rodriguez, M.-N. Antonopoulou, L. Isa, *Soft Matter* **2021**, *17*, 335.
[20] J. Menath, J. Eatson, R. Brilmayer, A. Andrieu-Brunsen, D. M. A. Buzza, N. Vogel, *Proc. Natl. Acad. Sci. U. S. A.* **2021**, *118*, e2113394118.
[21] N. Vogel, L. De Viguerie, U. Jonas, C. K. Weiss, K. Landfester, *Adv. Funct. Mater.* **2011**, *21*, 3064.
[22] F. Grillo, M. A. Fernandez-Rodriguez, M.-N. Antonopoulou, D. Gerber, L. Isa, *Nature* **2020**, *582*, 219.
[23] K. Volk, F. Deißenbeck, S. Mandal, H. Löwen, M. Karg, *Phys. Chem. Chem. Phys.* **2019**, *21*, 19153.
[24] A. D. Law, D. M. A. Buzza, T. S. Horozov, *Phys. Rev. Lett.* **2011**, *106*, 128302.
[25] Z. Dai, Y. Li, G. Duan, L. Jia, W. Cai, *ACS Nano* **2012**, *6*, 6706.
[26] J.-T. Zhang, L. Wang, D. N. Lamont, S. S. Velankar, S. A. Asherr, *Angew. Chem., Int. Ed.* **2012**, *51*, 6117.
[27] N. Vogel, S. Goerres, K. Landfester, C. K. Weiss, *Macromol. Chem. Phys.* **2011**, *212*, 1719.
[28] M. Kolle, P. M. Salgard-Cunha, M. R. J. Scherer, F. Huang, P. Vukusic, S. Mahajan, J. J. Baumberg, U. Steiner, *Nat. Nanotechnol.* **2010**, *5*, 511.
[29] N. Boechler, J. K. Eliason, A. Kumar, A. A. Maznev, K. A. Nelson, N. Fang, *Phys. Rev. Lett.* **2013**, *111*, 036103.
[30] B. Graczykowski, N. Vogel, K. Bley, H.-J. Butt, G. Fytas, *Nano Lett.* **2020**, *20*, 1883.
[31] C. L. Haynes, R. P. Van Duyne, *J. Phys. Chem. B* **2001**, *105*, 5599.
[32] M. Retsch, M. Tamm, N. Bocchio, N. Horn, R. Förch, U. Jonas, M. Kreiter, *Small* **2009**, *5*, 2105.
[33] A. Nemiroski, M. Gonidec, J. M. Fox, P. Jean-Remy, E. Turnage, G. M. Whitesides, *ACS Nano* **2014**, *8*, 11061.
[34] C. Stelling, C. Bernhardt, M. Retsch, *Macromol. Chem. Phys.* **2015**, *216*, 1682.
[35] K. Bley, J. Semmler, M. Rey, C. Zhao, N. Martic, R. N. Klupp Taylor, M. Stingl, N. Vogel, *Adv. Funct. Mater.* **2018**, *28*, 1706965.
[36] N. Vogel, R. A. Belisle, B. Hatton, T.-S. Wong, J. Aizenberg, *Nat. Commun.* **2013**, *4*, 2176.
[37] M. Karg, T. A. F. König, M. Retsch, C. Stelling, P. M. Reichstein, T. Honold, M. Thelakkat, A. Fery, *Mater. Today* **2015**, *18*, 185.
[38] R. Elnathan, B. Delalat, D. Brodoceanu, H. Alhmoud, F. J. Harding, K. Buehler, A. Nelson, L. Isa, T. Kraus, N. H. Voelcker, *Adv. Funct. Mater.* **2015**, *25*, 7215.
[39] T. Walter, A. Gruenewald, R. Detsch, A. R. Boccaccini, N. Vogel, *Langmuir* **2020**, *36*, 1793.
[40] M. Ã. Fernández-Rodríguez, R. Elnathan, R. Ditcovski, F. Grillo, G. M. Conley, F. Timpu, A. Rauh, K. Geisel, T. Ellenbogen, R. Grange, F. Scheffold, M. Karg, W. Richtering, N. H. Voelcker, L. Isa, *Nanoscale* **2018**, *10*, 22189.
[41] M. E. J. Hummel, C. Stelling, B. A. F. Kopera, F. A. Nutz, M. Karg, M. Retsch, S. Förster, *Langmuir* **2019**, *35*, 973.
[42] B. Ai, Y. Yu, H. Möhwald, G. Zhang, *Nanotechnology* **2013**, *24*, 035303.
[43] E. S. A. Goerlitzer, R. Mohammadi, S. Nechayev, K. Volk, M. Rey, P. Banzer, M. Karg, N. Vogel, *Adv. Mater.* **2020**, *32*, 2001330.
[44] G. Zhang, D. Wang, *J. Am. Chem. Soc.* **2008**, *130*, 5616.
[45] G. Zhang, D. Wang, H. Möhwald, *Nano Lett.* **2007**, *7*, 3410.
[46] F. J. Wendisch, M. Abazari, H. Mahdavi, M. Rey, N. Vogel, M. Musso, O. Diwald, G. R. Bourret, *ACS Appl. Mater. Interfaces* **2020**, *12*, 13140.
[47] M. Rey, F. J. Wendisch, E. S. Aaron Goerlitzer, J. S. Julia Tang, R. S. Bader, G. R. Bourret, N. Vogel, *Nanoscale Adv.* **2021**, *3*, 3634.
[48] F. J. Wendisch, M. S. Saller, A. Eadie, A. Reyer, M. Musso, M. Rey, N. Vogel, O. Diwald, G. R. Bourret, *Nano Lett.* **2018**, *18*, 7343.
[49] F. J. Wendisch, M. Rey, N. Vogel, G. R. Bourret, *Chem. Mater.* **2020**, *32*, 9425.
[50] Y. Brasse, V. Gupta, H. C. T. Schollbach, M. Karg, T. A. F. König, A. Fery, *Adv. Mater. Interfaces* **2020**, *7*, 1901678.
[51] K. Volk, J. P. S. Fitzgerald, M. Retsch, M. Karg, *Adv. Mater.* **2015**, *27*, 7332.
[52] L. Zhang, Z. Xiong, L. Shan, L.u Zheng, T. Wei, Q. Yan, *Small* **2015**, *11*, 4910.
[53] J. R. Oh, J. H. Moon, S. Yoon, C. R. Park, Y. R. Do, *J. Mater. Chem.* **2011**, *21*, 14167.

[54] K. Shinotsuka, Y. Kajita, K. Hongo, Y. Hatta, *Langmuir* **2015**, *31*, 11452.
[55] Q.-H. Wei, D. M. Cupid, X. L. Wu, *Appl. Phys. Lett.* **2000**, *77*, 1641.
[56] S. Ramananarivo, E. Ducrot, J. Palacci, *Nat. Commun.* **2019**, *10*, 3380.
[57] X. Meng, D. Qiu, *Langmuir* **2014**, *30*, 3019.
[58] P.-K. Kao, B. J. Vansaders, S. C. Glotzer, M. J. Solomon, *Sci. Rep.* **2021**, *11*, 11042.
[59] A. R. Barth, M. H. Martinez, C. E. Payne, C. G. Couto, I. J. Quintas, I. Soncharoen, N. M. Brown, E. J. Weissler, S. J. Gerbode, *Phys. Rev. E* **2021**, *104*, L052601.
[60] W. Khunsin, A. Aman, G. Kocher, S. Romanov, S. Pullteap, H. C. Seat, E. O'Reilly, R. Zentel, C. S. Torres, *Adv. Funct. Mater.* **2012**, *22*, 1812.
[61] E. S. A. Goerlitzer, R. N. Klupp Taylor, N. Vogel, *Adv. Mater.* **2018**, *30*, 1706654.
[62] R. Aveyard, J. H. Clint, D. Nees, V. N. Paunov, *Langmuir* **2000**, *16*, 1969.
[63] M. Retsch, Z. Zhou, S. Rivera, M. Kappl, X. S. Zhao, U. Jonas, Q. Li, *Macromol. Chem. Phys.* **2009**, *210*, 230.
[64] B. Van Duffel, R. H. A. Ras, F. C. De Schryver, R. A. Schoonheydt, *J. Mater. Chem.* **2001**, *11*, 3333.
[65] N. Francois, H. Xia, H. Punzmann, P. W. Fontana, M. Shats, *Nat. Commun.* **2017**, *8*, 14325.
[66] M. Faraday, *Philos. Trans. R. Soc. London* **1831**, *121*, 299.
[67] P. Chen, Z. Luo, S. Güven, S. Tasoglu, A. V. Ganesan, A. Weng, U. Demirci, *Adv. Mater.* **2014**, *26*, 5936.
[68] L. K. Migara, J.-K. Song, *NPG Asia Mater.* **2018**, *10*, e459.
[69] S.-H. Hong, J.-B. Gorce, H. Punzmann, N. Francois, M. Shats, H. Xia, *Sci. Adv.* **2020**, *6*, eaaz9386.
[70] M. Rey, X. Hou, J. S. J. Tang, N. Vogel, *Soft Matter* **2017**, *13*, 8717.
[71] J. Harrer, S. Ciarella, M. Rey, H. Löwen, L. M. C. Janssen, N. Vogel, *Soft Matter* **2021**, *17*, 4504.
[72] K. Volk, J. P. S. Fitzgerald, M. Karg, *ACS Appl. Mater. Interfaces* **2019**, *11*, 16096.
[73] J. S. J. Tang, R. S. Bader, E. S. A. Goerlitzer, J. F. Wendisch, G. R. Bourret, M. Rey, N. Vogel, *ACS Omega* **2018**, *3*, 12089.
[74] K. Geisel, L. Isa, W. Richtering, *Langmuir* **2012**, *28*, 15770.
[75] M. Rey, T. Yu, R. Guenther, K. Bley, N. Vogel, *Langmuir* **2019**, *35*, 95.
[76] E. Tjhung, L. Berthier, *Phys. Rev. E* **2017**, *96*, 050601(R).
[77] P. K. Hung, L. T. Vinh, D. M. Nghiep, P. N. Nguyen, *Computer Simulation of Liquid*, Clarendon Press, Oxford, UK **1987**.